Applied Catalysis B: Environment and Energy 375 (2025) 125415

Contents lists available at ScienceDirect

Applied Catalysis B: Environment and Energy

journal homepage: www.elsevier.com/locate/apcatb

Revealing the roles of oxidation states and constituents of the alloy in alkaline hydrogen evolution reaction

Xianjun Cao [a,b,1], Limeng Sun [a,1], Fengying Pan [a], Zeliang Wu [b], Dongfang Li [b], Xinming Nie [c,*], Xiaoyan Li [d], Peng Huang [e,*], Li Gao [a], Cheng Gong [a], Yufei Zhao [b,*], Qiong Cai [f], Jinqiang Zhang [b,*], Guoxiu Wang [b], Hao Liu [b,*]

[a] Joint International Laboratory on Environmental and Energy Frontier Materials, School of Environmental and Chemical Engineering, Shanghai University, Shanghai 200444, China
[b] Centre for Clean Energy Technology, Faculty of Science, University of Technology Sydney, Broadway, Sydney, NSW 2007, Australia
[c] School of Physics and Electronic Engineering, Jiangsu Normal University, Xuzhou, Jiangsu 221116, China
[d] Department of Electrical and Computer Engineering, University of Toronto, 35 St George Street, Toronto, Ontario M5S 1A4, Canada
[e] School of Chemistry and Materials Science, Jiangsu Normal University, Xuzhou, Jiangsu 221116, China
[f] School of Chemistry and Chemical Engineering, University of Surrey, Guildford, Surrey GU2 7XH, United Kingdom

ARTICLE INFO

Keywords:
Alkaline hydrogen evolution reaction
Capturing and releasing mechanism
Partial oxidation
PtRu alloy

ABSTRACT

Precious metal Pt has exhibited excellent catalytic performance in numerous electrocatalytic applications. However, the slow water dissociation kinetics hinder its alkaline hydrogen evolution reaction (HER) activity. Herein, we design the partially oxidized PtRu alloys with fine-tuned structure which can significantly enhance the alkaline HER. Theoretical calculations reveal that the alteration of Pt/Ru ratio and surface oxidation state of PtRu materials can effectively tune the water and hydrogen adsorption capability, thus impacting the alkaline HER performance. We dentify $Pt_{70}Ru_{30}$ with 3 O surface coverage with optimized adsorption energy to be the most suitable candidate for alkaline HER. Inspired by theoretical predictions, we prepare partially oxidized PtRu with tunable composition and structure via a facile urea-assisted method, with a "capture and release" reaction mechanism by generating complexing agents and pH gradients. The as-synthesized partially oxidized $Pt_{70}Ru_{30}$ electrode exhibits excellent HER catalytic activity and stability in the alkaline electrolyte, achieving an overpotential of only 11 mV at 10 mA cm^{-2} and a Tafel slope of 28 mV dec^{-1}, outperforming that of Pt/C (η_{10} = 29 mV, Tafel slope = 52 mV dec^{-1}). *In-situ* spectral measurements show that the partially oxidized Pt and Ru species in $Pt_{70}Ru_{30}$ can facilitate breaking the O-H bonds and improve the alkaline HER kinetics. This work unravels the influence of Pt/Ru ratio and surface partial oxidation on water dissociation and hydrogen adsorption, which provide guidelines for the rational design of highly efficient electrocatalysts.

1. Introduction

Renewable hydrogen energy is a highly promising secondary energy source that could potentially replace fossil fuels to meet the demands of future energy [1–6]. Electrochemical water splitting is widely regarded as an efficient method for green and sustainable hydrogen production [7,8]. While acidic water electrolysis based on proton exchange membrane (PEM) technology has significant advantages, its harsh operating conditions and sluggish anodic oxygen evolution reaction (OER) kinetics impede their further commercial application [9–11]. In contrast, alkaline water electrolysis presents a more practical option, offering cost-effectiveness and faster OER kinetics [12,13]. However, the hydrogen evolution reaction (HER) in alkaline media is two to three orders of magnitude slower than in acidic conditions due to the additional energy required for water dissociation [14–16]. Therefore, it is critical to design efficient electrocatalysts to boost the alkaline HER process for the overall alkaline water electrolysis.

The alkaline HER typically involves three key steps: water

* Corresponding authors.
E-mail addresses: nxinming@jsnu.edu.cn (X. Nie), huangpeng@jsnu.edu.cn (P. Huang), yufei.zhao@uts.edu.au (Y. Zhao), jinqiang.zhang@uts.edu.au (J. Zhang), hao.liu@uts.edu.au (H. Liu).
[1] These authors contributed equally to this work.

https://doi.org/10.1016/j.apcatb.2025.125415
Received 17 February 2025; Received in revised form 19 April 2025; Accepted 25 April 2025
Available online 27 April 2025

adsorption, water dissociation, and the adsorption of active intermediate H* species. The scarcity of protons in alkaline media requires their generation through the dissociation of adsorbed water. However, breaking the adsorbed H-OH bond involves a high reaction energy barrier. Furthermore, under alkaline conditions, the adsorption or desorption of the active intermediate H* or generated H_2 at the active sites are often either too weak or too strong, leading to suboptimal kinetic rates. To address these challenges, strategies such as introducing heteroatoms (both metals and non-metals), engineering defects, and designing hybrid structures (e.g., heterojunctions and tailored supports) to regulate the capability of H_2O adsorption/dissociation and H* adsorption/desorption can highly facilitate the alkaline HER process [17–22]. Specifically, Pt has long been considered the best electrocatalyst for HER due to its optimized H* binding energy [23–26]. However, the weak water activation capability of Pt necessitates the incorporation of oxophilic components, such as oxophilic metals, hydroxides, or oxides, to lower the energy barrier for water dissociation in alkaline environments. For instance, metal compounds like $Ni(OH)_2$ and CoO_x have been shown to facilitate water dissociation by cleaving H-OH bonds, thereby promoting the Volmer step and enhancing HER activity in alkaline media [27,28]. However, their low structural stability and sluggish charge transfer rate have impeded further improvements in performance. Alternatively, alloying Pt with other oxophilic metal elements, such as Ru, Ni, or Co, has been developed to enhance the water dissolution capability to achieve high alkaline HER activity. The synergistic effects between these elements lead to an adjustable electronic structure and improved stability, both critical for optimizing the multistep alkaline HER process. Among these candidates, the relatively low-cost Ru ($42 per ounce) possesses similar hydrogen bonding strength to Pt and low water dissociation energy barriers, which can contribute to optimized adsorption energy for the intermediates, resulting in enhanced alkaline HER. Several studies have explored PtRu alloys, such as PtRu nanoclusters with Pt-Ru bridge structures, Ru-modified Pt step edges, and torsionally strained PtRu mesocrystals (PtRu MCs), all of which exhibit high activity for alkaline HER [29–31]. However, a comprehensive understanding of the atomic structure, catalytic roles, and reaction mechanisms within these bimetallic systems remains incomplete, highlighting the need for further investigation to optimize their electrochemical performance.

Moreover, the chemical state, particularly the oxidation state of active metals, is an important factor that influences catalytic activity in alkaline hydrogen evolution reactions (HER). Studies have shown that metal centers with lower oxidation states are often more favorable for H* adsorption, resulting in enhanced catalytic performance [32,33]. For instance, negatively charged $Pt^{\delta-}$ in Pt/MgO tends to accumulate a higher concentration of H_3O^+ intermediates, demonstrating superior HER activity compared to 20 wt% Pt/C [34]. Similarly, partially reduced Ru/RuO_2 composites exhibit excellent water adsorption and dissociation, along with optimal H and OH binding energies at the interface, further boosting catalytic activity [35]. On the other hand, there are also reports suggesting that metal centers with higher oxidation states can also improve catalytic performance. For instance, Ru with a higher oxidation state (Ru^{n+}) in Au@Ru has been shown to outperform low-valent Ru (0) for alkaline HER, as the higher oxidation state of Ru provides a more balanced adsorption capacity for interfacial water, H* , and OH* [36]. Therefore, given the conflicting reports on the role of oxidation states in catalytic activity, it is crucial to further investigate and clarify their impact, along with the underlying catalytic mechanisms.

Herein, we design PtRu bimetallic electrocatalysts with tunable composition and oxidation state to precisely optimize the water adsorption and hydrogen bonding energies for alkaline HER. Density functional theory (DFT) calculations show that the optimized Pt/Ru ratio with moderate surface oxidation can not only highly reduce the energy barrier of rate-determining step (RDS) for alkaline HER, but also induce both Pt and Ru species work as the active sites for water adsorption and H* reaction. Inspired by this theoretical prediction, we employed a simple urea-decomposition-assisted method to synthesize partially oxidized PtRu alloys with tunable composition, morphology, and oxidation states for superior alkaline HER performance. In this method, urea acts as a precursor, releasing NH_3 and CO_2 under high temperature and pressure. The generated NH_3 captures Pt^{4+} and Ru^{3+} ions, forming $Pt(NH_3)_2^{2+}$ and $Ru(NH_3)_6^{3+}$ complexes, thereby slowing their deposition rate and promoting the formation of a unique alloy architecture. Meanwhile, the CO_2 disperses in the solution, creating a pH gradient that modulates Pt^{4+} deposition and leads to an optimized Pt/Ru ratio. This method allows precise control over morphology and elemental composition, resulting in varied surface metal atom exposure and oxidation states, as well as O coverage. By adjusting the amount of urea to 0.250 mmol, we achieved a two-dimensional (2D) porous sheet-like structure composed of uniformly distributed nanoparticles with optimal oxidation states. This structure exhibited an overpotential of just 11 mV at a current density of 10 mA cm^{-2} and a low Tafel slope of 28 mV dec^{-1}, outperforming commercial Pt/C (η_{10} = 29 mV, Tafel slope = 52 mV dec^{-1}). This study demonstrates the critical role of PtRu's chemical state, including composition and oxidation state, in enhancing alkaline HER performance, providing valuable insights for the rational design of efficient water-splitting electrocatalysts.

2. Experimental section

2.1. Materials

Chemicals and Materials. Chloroplatinic acid hexahydrate ($H_2PtCl_6{\cdot}6H_2O$, 99.95 %), Ruthenium (III) Chloride ($RuCl_3$, 99.5 %) were purchased from Adamas. Urea, Sodium Hydroxide (NaOH), potassium hydroxide (KOH) and ethanol (CH_3CH_2OH) were purchased from Greagent. Polyvinylpyrrolidone (PVP, Mw = 450000–550000) was purchased from Sinopharm Chemical Reagent Co., Ltd. (Shanghai, China). Nafion perfluorinated resin (5 wt%) was obtained from Sigma-Aldrich. The carbon black (Vulcan XC-72) was obtained Cabot. All reagents were of analytical reagent grade and used without further purification.

2.2. Synthesis of PO-$Pt_{70}Ru_{30}$

PO-$Pt_{70}Ru_{30}$ was prepared by hydrothermal method. Firstly, 0.0388 g $H_2PtCl_6{\cdot}6H_2O$ (0.0075 mmol), 0.0052 g $RuCl_3$ (0.025 mmol) and 0.0150 g urea (0.250 mmol) were added into 7.0 mL deionized water with continuous ultrasonic for 30 minutes at room temperature. The molar ratio of Pt/Ru/urea is 3/1/10. After that, 30 mg of PVP was added into the above solution for another 30 min sonication. Finally, the pH was adjusted to 12 with NaOH solution. The resulting solution was transferred to a 20 mL Teflon-lined stainless steel autoclave and heated at 140 °C for 4 h. After cooling to room temperature, the precursor of $Pt_{70}Ru_{30}$ was obtained by centrifugation, washing with water and ethanol, and vacuum drying at 80 °C. The precursor was then heated in a muffle furnace from room temperature to 400 °C for annealing to obtain PO-$Pt_{70}Ru_{30}$.

For comparison, PO-$Pt_{90}Ru_{10}$, PO-$Pt_{80}Ru_{20}$ and PO-$Pt_{60}Ru_{40}$ with different urea contents were also prepared, in which the urea molar amounts were 0.050 mmol, 0.125 mmol and 0.375 mmol, respectively. Reduced and further oxidized PO-$Pt_{70}Ru_{30}$ (named $Pt_{70}Ru_{30}$-reduced and $Pt_{70}Ru_{30}$-oxidized) have been achieved by heat treatment in H_2/Ar and air for 2 h, respectively.

2.3. Material characterizations

The crystal structures of PO-$Pt_{90}Ru_{10}$, PO-$Pt_{80}Ru_{20}$, PO-$Pt_{70}Ru_{30}$ and PO-$Pt_{60}Ru_{40}$ samples were collected on a 18KW D/MAX2500V X-ray diffractometer (XRD). The morphology and structure of PO-$Pt_{90}Ru_{10}$, PO-$Pt_{80}Ru_{20}$, PO-$Pt_{70}Ru_{30}$ and PO-$Pt_{60}Ru_{40}$ samples were observed by

JEOL 2100 F transmission electron microscope (TEM), where the accelerating voltage was 200 kV. High-angle annular dark-field scanning transmission electron microscopy (HAADF-STEM) images and energy-dispersive X-ray spectroscopy (EDX) were obtained with a JEM-ARM300F double spherical aberration-corrected transmission electron microscope. XAFS (Pt L_3-edge and Ru K-edge) spectra were acquired at the BL14W1 station of the Shanghai Synchrotron Radiation Facility (SSRF, storage ring operated at 3.5 GeV with a maximum current of 250 mA). X-ray photoelectron spectra (XPS) of the samples were collected on a Thermo Scientific K-Alpha. The element contents of Pt and Ru in PO-$Pt_{90}Ru_{10}$, PO-$Pt_{80}Ru_{20}$, PO-$Pt_{70}Ru_{30}$ and PO-$Pt_{60}Ru_{40}$ samples were characterized by ICP-OES model Agilent 7700.

2.4. Electrochemical measurements

The alkaline HER performance of PO-$Pt_{90}Ru_{10}$, PO-$Pt_{80}Ru_{20}$, PO-$Pt_{70}Ru_{30}$ and PO-$Pt_{60}Ru_{40}$ and commercial Pt/C catalysts were tested at room temperature using a three-electrode system connected to a CHI 760E electrochemical workstation. The working electrode is a glassy carbon rotating disk electrode (RDE, with a geometric area of 0.196 cm^{-2}), and the Hg/HgO electrode and the carbon rod electrode are the reference electrode and the counter electrode, respectively. 1 mg of the PtRu material catalyst was dispersed in a mixed solution of 135 μL isopropanol, 15 μL ethanol and 10 μL Nafion (5 wt%) and sonicated for 2 h to obtain a uniformly mixed ink. Pipette 2 μL solution from the black ink to load on the working electrode (loading capacity is 0.0637 mg cm^{-2}). After drying at room temperature, the three electrodes were inserted into 1 M KOH solution for electrochemical testing. The potential measured electrochemically needs to be converted by the reversible hydrogen electrode (Eq. (1)):

$$E_{RHE} = E_{Hg|Hgo} + 0.059*pH + 0.098 \quad (1)$$

Linear sweep voltammetry (LSV) was obtained at a potential range of 0.10∼-0.20 V vs RHE and a scan rate of 5 mV s^{-1}. All potentials in LSV are iR corrected. Electrochemical impedance (EIS) was obtained under the parameter settings of frequency 0.01∼10^5 Hz, amplitude 5 mV, voltage 2 mV vs RHE. The electrochemically active specific surface area (ECSA) was measured by cyclic voltammetry (CV) at a scan rate of 50 mV s^{-1} over a voltage range of V vs RHE. The stability of the catalyst was tested by chronoamperometry and CV. CV stability was characterized for 5000 cycles at a scan rate of 50 mV s^{-1} over a voltage range of -0.15∼0.05 V vs. RHE. The TOF value was calculated based on the following equation: (Eq. (2)):

$$TOF(s^{-1}) = \frac{j*S}{n*F*N} \quad (2)$$

where j represents the current density (mA cm^{-2}), S is for the geometric area of a GCE (0.196 cm^{-2}), n is the number of electron transfers (n = 2), and F is Faraday's constant (96485.3 C mol^{-1}). All metal sites have been assumed as active sites for alkaline HER.

2.5. In situ ATR-SEIRAS measurements

PO-$Pt_{70}Ru_{30}$, $Pt_{70}Ru_{30}$-reduced and $Pt_{70}Ru_{30}$-oxidized coated Au/Si was used as the working electrode with an Ag/AgCl and a carbon rod being the reference and counter electrodes, respectively. Briefly, ATR-SEIRA spectra were acquired at a resolution of 4 cm^{-1} with unpolarized IR radiation at an incidence angle of ca. 70° by a Nicolet iS50 FT-IR spectrometer with a built-in MCT detector. All the spectra are shown in the absorbance unit as -log(I/I_0), where I and I_0 represent the intensities of the reflected radiation of the sample and reference spectra, respectively. Poterntiodynamic ATR-SEIRAS spectra on PO-$Pt_{70}Ru_{30}$, $Pt_{70}Ru_{30}$-reduced and $Pt_{70}Ru_{30}$-oxidized were performed in N_2-saturated KOH solution with potentials from -1.5∼-0.9 V vs RHE and a scan rate of 5 mV s^{-1}.

2.6. In situ electrochemical Raman measurements

The operando Raman spectra were collected on a HORIBA XploRA PLUS Raman spectrometer with an electrochemical cell, catalysts with carbon black were directly dropped on glassy carbon plate as the working electrode, calomel electrode and carbon rod were used as the reference electrode and counter electrode, respectively. It operated from 3000 to 4000 cm^{-1} and 0 to -0.5 V vs. RHE in 1 M KOH solution to evaluate the water dissociation ability of catalysts.

2.7. Density-functional theory calculation

Density-functional theory (DFT) calculations used the Vienna Ab initio Simulation Package (VASP) to calculate the binding energy for specific surfaces of catalysts. The Perdew, Burke and Ernzerhof (PBE) parameterized generalized exchange-correlation interactions are implemented by the VASP package. A cutoff energy of 400 eV was used in all calculations. A (3 × 3 × 2) Monkhorst-Pack k-point sampling were used for all surface calculations and boxes of 15 Å × 15 Å × 15 Å have been used for H_2O and H_2 calculation. In this study, we set a vacuum layer and calculated the H* adsorption energy and water dissociation energy of alloy materials with different Pt/Ru ratios by ignoring the solvation effect. The optimal Pt/Ru ratio was determined by using the H* adsorption energy and water dissociation energy descriptors. Based on this, we covered the surface with different amounts of O coverage and further calculated the H* adsorption energies and water dissociation energies. It is worth noting that the surface 3 O coverage is close to the fitting of the PO-$Pt_{70}Ru_{30}$ X-ray absorption spectrum. We approximately use $Pt_{70}Ru_{30}$-3O as the calculation model of PO-$Pt_{70}Ru_{30}$.

3. Results and discussion

3.1. Theoretical predictions

DFT calculations were performed to investigate the influence of composition and oxidation state on the adsorption properties and electronic features of PtRu alloys for alkaline hydrogen evolution reaction (HER). First, we focused on the Pt(111) surface and PtRu alloys with varying Ru doping levels of 0 %, 15 %, 30 %, 45 %, 60 %, and 100 %. The adsorption energies of H_2O (ΔG_{H2O}) and H* (ΔG_{H^*}) were calculated for each model-including pure Pt, pure Ru, and PtRu alloys-to assess their potential for alkaline HER. As shown in Fig. 1a and Table S2, increasing the Ru content in PtRu alloys significantly improves H_2O adsorption capacity, suggesting that initial H_2O adsorption may preferentially occur on Ru sites during alkaline HER. Specifically, PtRu alloys with 30 %, 45 %, and 60 % Ru exhibited similar H_2O adsorption energies of -0.20 eV, -0.21 eV, and -0.20 eV, respectively. In contrast, the H* adsorption energy across the Pt, PtRu, and Ru series increased from -0.10 eV for Pt to -0.42 eV for pure Ru. A higher ΔG_{H^*} hinders hydrogen release, which ultimately reduces HER activity. Based on these findings, the PtRu alloy with 30 % Ru demonstrated the most balanced adsorption energies for both H_2O (-0.20 eV) and H* (-0.22 eV), identifying it as the optimal composition for alkaline HER. DFT calculations were performed to determine the adsorption energies of H_2O and H* on Pt and Ru sites in the $Pt_{70}Ru_{30}$ alloy (Fig. S11a). The results reveal that H_2O adsorption is significantly weaker on Pt sites (0.18 eV) than on Ru sites (-0.20 eV). Similarly, H* exhibits slightly stronger adsorption on Ru (-0.27 eV) compared to Pt (-0.22 eV). These findings suggest that in $Pt_{70}Ru_{30}$, Ru acts as the primary site for H_2O adsorption, while the generated H* migrates to adjacent Pt sites for hydrogen evolution, consistent with previously reported mechanisms in bimetallic systems [37–39]. We further explored the effect of oxidation states by introducing different surface oxygen coverages on the optimized $Pt_{70}Ru_{30}$ alloy. Fig. 1b and Table S3 show that as surface oxygen coverage increases, the H_2O adsorption capacity of $Pt_{70}Ru_{30}$ weakens. However, the H* adsorption energy exhibits a volcano plot trend, with the optimal

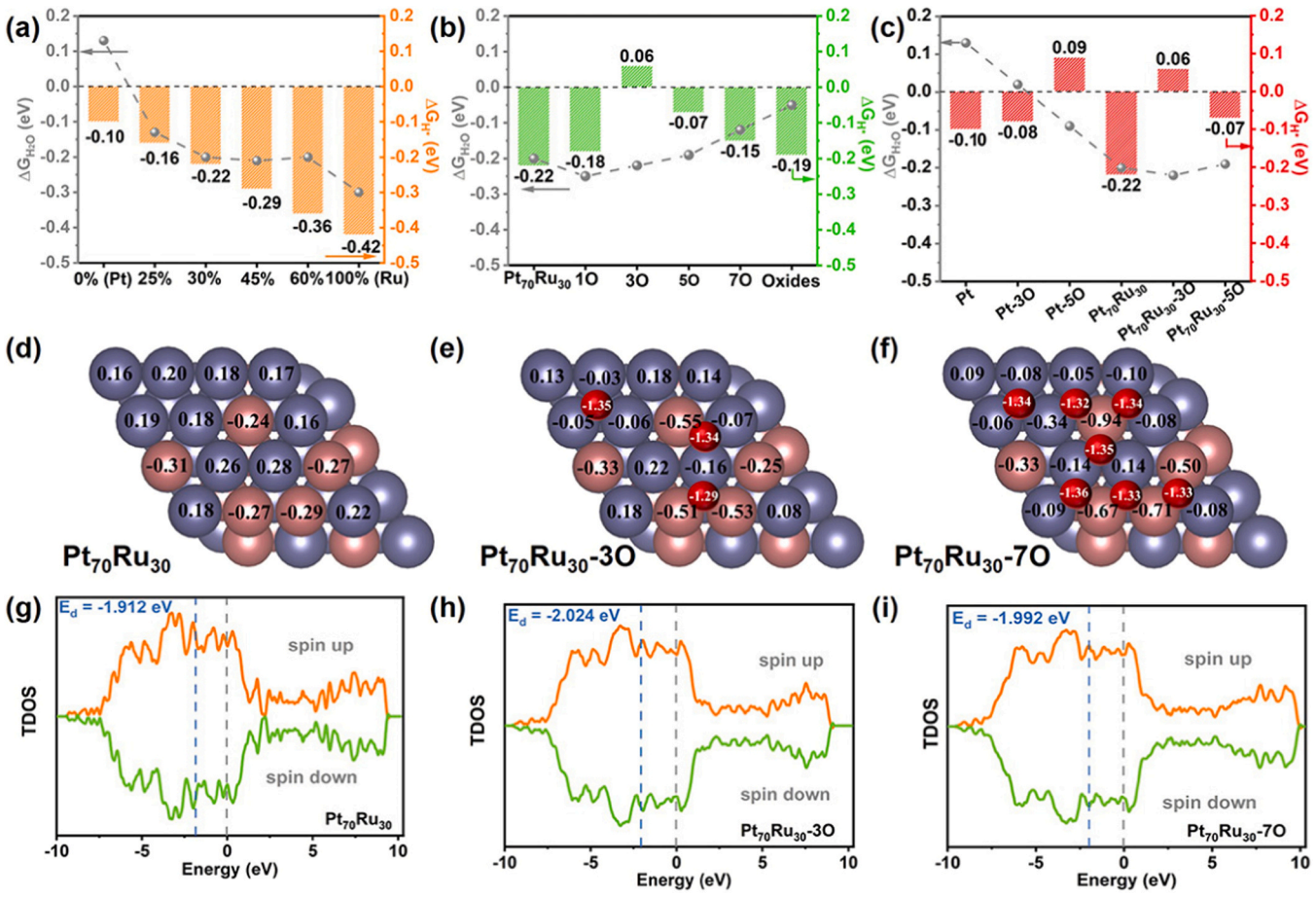

Fig. 1. Theoretical simulations. (a) Adsorption free energy of H_2O ($\triangle G_{H2O}$) and H* ($\triangle G_{H^*}$) on PtRu alloys with different Ru doping amounts. (b) Adsorption free energy of H_2O ($\triangle G_{H2O}$) and H* ($\triangle G_{H^*}$) on the $Pt_{70}Ru_{30}$ surface at different oxidation degrees (the oxidation degree increases from 1O, 3O , 5O , 7O and complete oxidation). (c) Adsorption free energy of H_2O ($\triangle G_{H2O}$) and H* ($\triangle G_{H^*}$) on the Pt, Pt-3O, Pt-5O, $Pt_{70}Ru_{30}$, $Pt_{70}Ru_{30}$-3O and $Pt_{70}Ru_{30}$-5O surface. (d-f) The Bader charge numbers of atoms in $Pt_{70}Ru_{30}$, $Pt_{70}Ru_{30}$-3O and $Pt_{70}Ru_{30}$-7O. Note that the negative value is referred to obtain electrons, while the positive value means to lose electrons. Gray, orange and red balls represent Pt, Ru and O atoms, respectively. (g-i) TDOS profiles of $Pt_{70}Ru_{30}$, $Pt_{70}Ru_{30}$-3O and $Pt_{70}Ru_{30}$-7O.

H* adsorption energy of 0.06 eV occurring at a surface coverage of 3O , which is close to the theoretical ideal ($\Delta G_{H^*} = 0$ eV). Therefore, $Pt_{70}Ru_{30}$ with 3 O surface coverage (referred to as $Pt_{70}Ru_{30}$-3O) is predicted to exhibit the highest catalytic potential for alkaline HER based on these DFT calculations. It is worth noting that the high catalytic activity of $Pt_{70}Ru_{30}$-3O originates from the synergistic effects between the Pt/Ru composition and oxidation states, which is verified by performing additional calculations on the pure Pt. We identify that altering the oxidation state of the pure Pt surface has a relatively minor impact on the binding energies of H_2O and H* compared to PtRu alloys. For example, Pt-3O and Pt-5O exhibit similar low H_2O adsorption energies and optimized H* adsorption energies to that of pure Pt (Fig. 1c). In contrast, the introduction of Ru and oxygen significantly enhances the H_2O adsorption capability on Pt atoms. To further elucidate the respective roles of Ru and Pt in $Pt_{70}Ru_{30}$-3O, we performed DFT calculations to evaluate the adsorption energies of H_2O and H* on Pt and Ru sites (Fig. S11a, c). The results show that H_2O adsorption energy on Pt sites (-0.22 eV) is comparable to that on Ru sites (-0.22 eV), while H* adsorption energy on Ru (-0.07 eV) is similar to that on Pt (0.06 eV). These results suggest that there is a positive interaction between partially oxidized Pt and Ru in $Pt_{70}Ru_{30}$-3O, making both partially oxidized Pt and Ru species serve as active sites for H_2O adsorption and H* generation, thereby synergistically enhancing the alkaline HER kinetics. Since water dissociation is the rate-limiting step in alkaline HER, the calculated energy barrier (ΔG_B, Fig. S11b) for water decomposition on the metallic Pt surface is relatively high ($\Delta G_B = 0.95$ eV), which hinders the breaking of the OH-H bond and the formation of H* intermediates, resulting in poor alkaline HER activity. Introducing Ru significantly lowers this barrier, with $Pt_{70}Ru_{30}$ exhibiting a reduced energy barrier of 0.69 eV. Notably, further modification to form $Pt_{70}Ru_{30}$-3O decreases the barrier even more, down to 0.53 eV. However, excessive oxidation, as in $Pt_{70}Ru_{30}$-7O, increases the energy barrier to 0.86 eV. The above results indicate that incorporation of Ru and moderate O coverage play a crucial role in promoting water dissociation and thus improving the alkaline HER catalytic performance.

To further elucidate the advantages of $Pt_{70}Ru_{30}$ with 3O surface coverage, we investigated the detailed electronic structures of the PtRu alloy, $Pt_{70}Ru_{30}$-3O, and $Pt_{70}Ru_{30}$-7O. The Bader charge calculation results show that in the PtRu alloy, Pt atoms are positively charged, while Ru atoms are negatively charged, which can promote the transfer of electrons from Pt atoms to adjacent surface Ru atoms (Fig. 1d). [40,41]. However, compared with $Pt_{70}Ru_{30}$, $Pt_{70}Ru_{30}$-3O and $Pt_{70}Ru_{30}$-7O after the introduction of oxygen atoms show different charge redistribution. The Pt atoms adjacent to the oxygen atoms are negatively charged, while the Pt atoms relatively far away from the oxygen atoms are still positively charged but with a reduced charge number. Affected by Ru and O atoms, Pt charge redistribution can enhance H* adsorption, thereby accelerating the HER process (Fig. 1e, f). [42,43]. Pt atoms far away from O atoms still present positive charge states, which is conducive to the adsorption of negative O in H_2O [44,45]. This phenomenon may be attributed to secondary electron transfer between Pt atoms near oxygen due to the significant electronegativity difference between Pt and O. The

chemical bonds between Pt and O cause electrons to be drawn towards the O atoms, facilitating a secondary electron transfer from surrounding atoms to the electron-deficient Pt atoms. This leads to an increase in charge density on Pt atoms close to O and a decrease in charge density on those further away. As the oxygen coverage on the $Pt_{70}Ru_{30}$ surface increases, the number of positively charged Pt atoms decreases, which suppresses H_2O adsorption (Fig. 1c). Additionally, the total density of states (TDOS) for $Pt_{70}Ru_{30}$, $Pt_{70}Ru_{30}$-3O, and $Pt_{70}Ru_{30}$-7O, shown in Fig. 1g-i, reveals strong DOS intensity at the Fermi level, confirming excellent conductivity and fast charge transfer. $Pt_{70}Ru_{30}$-3O exhibits a decreased d-band center (E_d) of -2.024 eV, lower than that of the PtRu alloy (-1.912 eV) and $Pt_{70}Ru_{30}$-7O (-1.992 eV). This lower E_d on the negatively charged Pt surface weakens H* adsorption energy, a critical factor in enhancing HER catalytic activity. Therefore, during the alkaline HER process, a rapid water adsorption/dissociation process occurred at the Ru/Pt sites on the PO-$Pt_{70}Ru_{30}$ surface, generating abundant H* , which in turn catalyzed rapid H_2 production.

3.2. Catalysts synthesis and characterization

Inspired by the theoretical predictions, partially oxidized PtRu was synthesized using a urea decomposition-assisted hydrothermal method (Fig. 2a). During the process, urea decomposition under highly alkaline hydrothermal conditions releases a mixture of NH_3 and CO_2 gases ($(NH_2)_2CO + H_2O \rightarrow 2NH_3 + CO_2$). The gas mixture rapidly forms bubbles in the solution, which serve as templates for PtRu growth. Simultaneously, the generated CO_2 and NH_3 adjust the local microenvironment around the templates, allowing for the optimal deposition rate of Pt^{2+} and Ru^{3+} to achieve the desired $Pt_{70}Ru_{30}$ composition [46,47]. The target partially oxidized PtRu materials are achieved after the quick treatment at 400 °C.

It has been demonstrated that the amount of urea used during the hydrothermal reaction plays a crucial role in determining the final morphology and composition of partially oxidized PtRu materials. A series of experiments were conducted under identical conditions, varying the amount of urea. Different Pt/Ru ratios ($Pt_{90}Ru_{10}$, $Pt_{80}Ru_{20}$, $Pt_{70}Ru_{30}$, and $Pt_{60}Ru_{40}$) were achieved by adjusting the urea molar amounts from 0.05 mmol, 0.125 mmol, 0.250 mmol, to 0.375 mmol, as confirmed by ICP-OES (Fig. 2c). TEM images in Fig. 2b show that the morphology evolves with increasing urea content. For partially oxidized $Pt_{90}Ru_{10}$ (PO-$Pt_{90}Ru_{10}$), a spherical structure with an average size of ~60 nm, composed of small nanoparticles with an average size of about 2.37 nm, is observed (Fig. 2bi and Fig. S12a). As the urea concentration increases, a mixed morphology of spheres and sheet-like structures appears (Fig. 2bii). When the amount of urea reaches 0.250 mmol, a uniform 2D sheet-like structure consisting of evenly distributed nanoparticles (~2.32 nm) is formed for partially oxidized $Pt_{70}Ru_{30}$ (PO-$Pt_{70}Ru_{30}$)(Fig. 2biii and Fig. S12c). However, further increasing the urea beyond 0.250 mmol results in randomly distributed nanoparticles (~2.66 nm) for partially oxidized $Pt_{60}Ru_{40}$ (PO-$Pt_{60}Ru_{40}$)(Fig. 2biv and Fig. S12d), indicating that the correct amount of urea is critical for achieving the desired morphology in partially oxidized PtRu materials.

The XRD spectra in Fig. 2d show that all dominant peaks of the partially oxidized PtRu materials PO-$Pt_{90}Ru_{10}$, PO-$Pt_{80}Ru_{20}$, PO-$Pt_{70}Ru_{30}$, and PO-$Pt_{60}Ru_{40}$ are located between the diffraction points of metallic Pt and Ru. As the amount of urea increases, these peaks exhibit

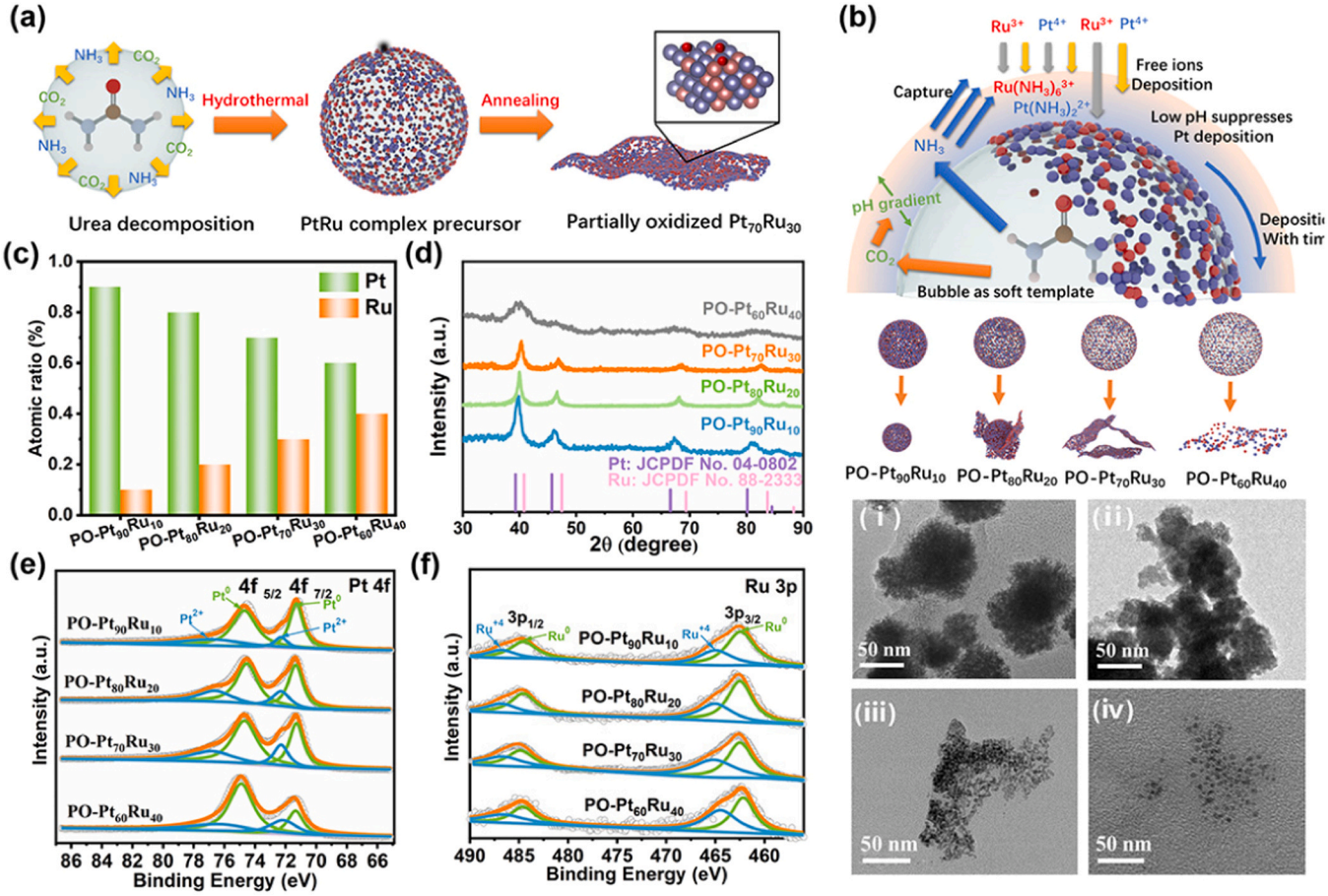

Fig. 2. Structural characterizations. (a) Schematic diagram of the synthesis process of PO-$Pt_{70}Ru_{30}$. (b) Schematic illustration of the formation mechanism and (i, iii, iii, iv) TEM images of PO-$Pt_{90}Ru_{10}$, PO-$Pt_{80}Ru_{20}$, PO-$Pt_{70}Ru_{30}$ and PO-$Pt_{60}Ru_{40}$. (c) ICP-OES results and (d) XRD spectra of PO-$Pt_{90}Ru_{10}$, PO-$Pt_{80}Ru_{20}$, PO-$Pt_{70}Ru_{30}$ and PO-$Pt_{60}Ru_{40}$. High-resolution XPS spectra of (e) Pt 4 f and (f) Ru 3p in PO-$Pt_{90}Ru_{10}$, PO-$Pt_{80}Ru_{20}$, PO-$Pt_{70}Ru_{30}$ and PO-$Pt_{60}Ru_{40}$.

a positive shift toward the position of Ru, indicating increased incorporation of Ru into the alloy (the XRD spectrum of PO-$Pt_{70}Ru_{30}$ before annealing is shown in Fig. S14a). Notably, PO-$Pt_{60}Ru_{40}$ exhibits the lowest XRD peak intensity among the samples, suggesting poor crystallinity due to the presence of small, randomly distributed nanoparticles. We further conducted XPS to investigate the surface electronic structure and chemical composition of the partially oxidized PtRu materials. The surface Pt content gradually decreases from 0.79 to 0.26, while the Ru content correspondingly increases from 0.21 to 0.74, as shown in Fig. S15. These trends are consistent with the ICP-OES results. The fitted high-resolution Pt 4 f and Ru 3p XPS spectra (Figs. 2e and 2f) reveal the presence of Pt^0/Pt^{2+} and Ru^0/Ru^{4+} species due to surface oxidation. Additionally, the proportions of Pt^{2+} and Ru^{4+} increase progressively from PO-$Pt_{90}Ru_{10}$ to $Pt_{60}Ru_{40}$. This demonstrates that the morphology and composition of the partially oxidized PtRu materials significantly influence the oxidation states of Pt and Ru after rapid high-temperature treatment. In addition, from PO-$Pt_{90}Ru_{10}$ to PO-$Pt_{60}Ru_{40}$, the Pt 4 f binding energy gradually shifts positively, while the Ru 3p binding core energy gradually shifts negatively, which further indicates increased enhances the electron transfer from Pt to Ru for the partially oxidized PtRu.

Based on the results, the partially oxidized PtRu materials were synthesized through a "capture and release" reaction pathway, facilitated by urea decomposition and heat treatment. The release of CO_2 and NH_3 gases from urea decomposition plays a key role in forming the PtRu alloy. The CO_2 and NH_3 gas mixture serves as a soft bubble template for alloy growth, promoting the nucleation of Pt and Ru. Additionally, the dispersion of these gases in the solution helps regulate the microenvironment around the soft template. NH_3, a strong complexing agent, readily "captures" free Pt^{2+} and Ru^{4+} ions, reducing their precipitation. At lower urea concentrations, less NH_3 is released, resulting in only a small amount of Pt^{2+} and Ru^{4+} being captured around the soft template to form $Pt(NH_3)_2^{2+}$ and $Ru(NH_3)_6^{3+}$ complexes. Meanwhile, a larger proportion of Pt^{2+} and Ru^{4+} ions are rapidly reduced, forming large spherical structures. As the urea concentration increases, more NH_3 is released, capturing more Pt^{2+} and Ru^{4+}, which decreases the amount of free metal ions around the soft template and reduces the precipitation rate. This leads to insufficient material to fully cover the bubble template, resulting in the breakdown of the spherical structure and the formation of a lamellar morphology (Fig. 2b) [48,49]. The CO_2 released by the decomposition of urea forms a pH gradient around the template, which inhibits the reduction of Pt^{4+}, thereby optimizing the composition of PtRu [50]. As the urea content increases, the morphology of the PtRu alloy shifts from a dense spherical structure to a fragmented,

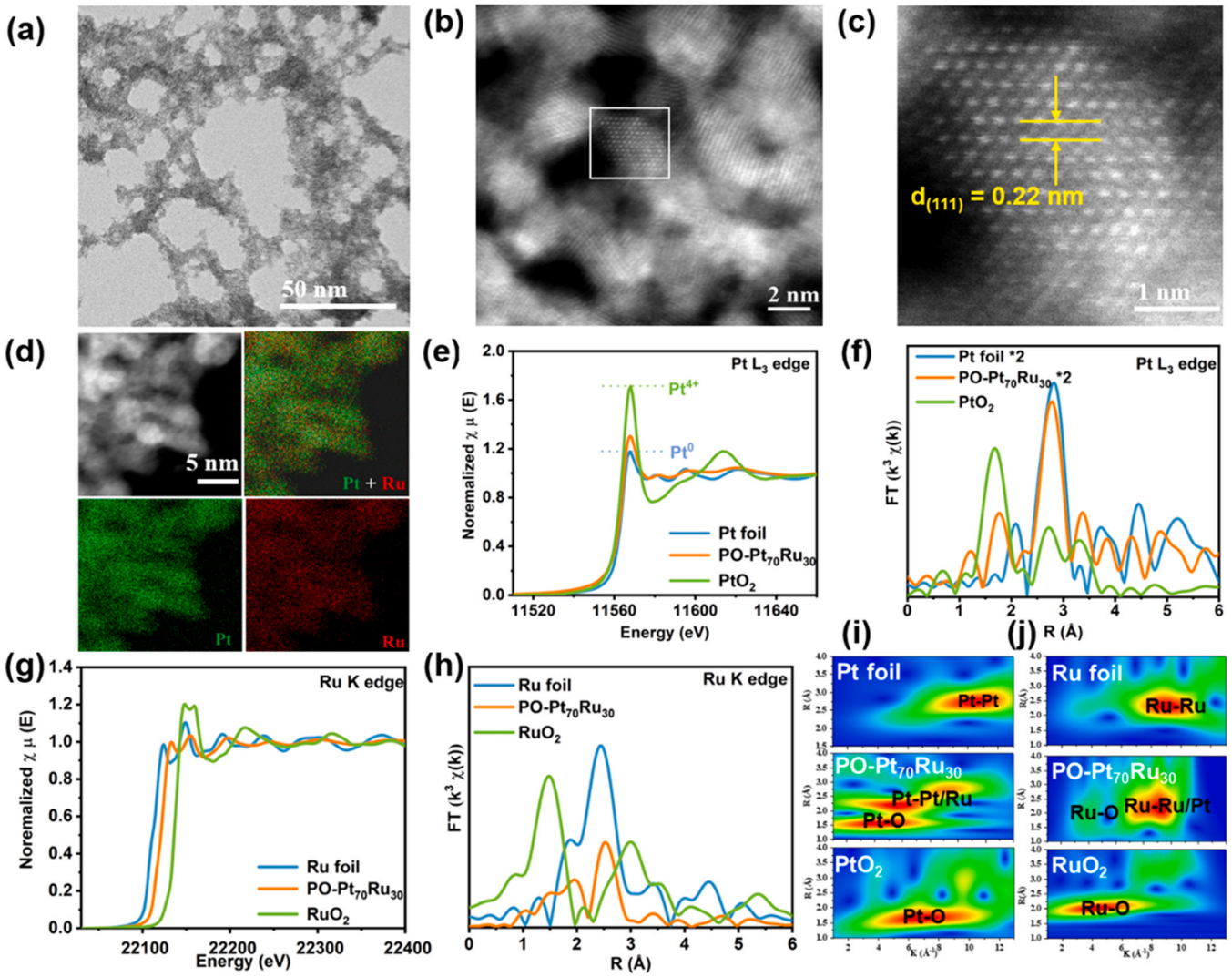

Fig. 3. Compositional structure analysis. (a) TEM and (b, c) HAADF-STEM images of PO-$Pt_{70}Ru_{30}$. (d) HAADF-STEM-EDX mapping of Pt and Ru in PO-$Pt_{70}Ru_{30}$ alloy. (e-f) XANES and EXAFS spectra at Pt L_3-edge of PO-$Pt_{70}Ru_{30}$, Pt foil and PtO_2. (g-h) XANES and EXAFS spectra at Ru K-edge of PO-$Pt_{70}Ru_{30}$, Ru foil and RuO_2. (i-j) EXAFS wavelet transform plots of Pt L_3-edge for Pt foil, PO-$Pt_{70}Ru_{30}$, PtO_2, and Ru K-edge for Ru foil, PO-$Pt_{70}Ru_{30}$, RuO_2.

flake-like structure, leading to a higher number of exposed surface atoms. These exposed atoms are more easily oxidized during thermal treatment, which results in a progressive increase in the oxidation state from PO-$Pt_{90}Ru_{10}$ to PO-$Pt_{60}Ru_{40}$. The two-step synthesis process-urea-assisted "capture and release" followed by thermal treatment-optimizes the morphology, composition, and oxidation state of the partially oxidized PtRu materials, thus achieving enhanced HER activity.

Based on the DFT calculations and experimental results, the optimized PO-$Pt_{70}Ru_{30}$ was further characterized using TEM and HAADF-STEM. HAADF-STEM images in Fig. 3b and c clearly reveal that PO-$Pt_{70}Ru_{30}$ alloy exhibits distinct lattices and high crystallinity. The measured lattice spacing of 0.22 nm is slightly smaller than the standard lattice spacing of 0.226 nm on the Pt (111) crystal plane. This further demonstrates the formation of alloy by replacing the Pt atoms with the smaller Ru atoms, which is consistent with the XRD results [51–53]. The EDX spectrum of the PO-$Pt_{70}Ru_{30}$ alloy confirms the presence of both Pt and Ru (Fig. S18), while the elemental mapping images in Fig. 3d demonstrate their uniform distribution across the material, with no signs of aggregation.

We further investigated the electronic structure and coordination environment of the PO-$Pt_{70}Ru_{30}$ alloy using XAS. Fig. 3e shows the normalized Pt L_3-edge X-ray absorption near-edge structure (XANES) with reference to standard Pt foil and PtO_2. The intensity of the Pt L_3-edge white line (WL) in PO-$Pt_{70}Ru_{30}$ is between that of Pt foil and PtO_2, indicating that the Pt in PO-$Pt_{70}Ru_{30}$ is positively charged with oxidation states between 0 and + 4. The average valence state of Pt can be quantitatively detected by integration of the white line peak in the differential XANES spectrum (ΔXANES) [37,54,55]. The calculated results indicate that the average valence state of Pt in PO-$Pt_{70}Ru_{30}$ is 0.75 (Fig. S20a). This relatively low valence state suggests an increase in the d-band electrons of Pt, which is advantageous for enhancing HER performance [25,56–58]. The normalized XANES of the Ru K-edge (Fig. 3g) shows that the absorption threshold position of PO-$Pt_{70}Ru_{30}$ is higher than that of Ru foil but lower than that of RuO_2. The average valence state of Ru in PO-$Pt_{70}Ru_{30}$ is calculated to be approximately + 1.39 (Fig. S20b). The coordination environments of Pt and Ru atoms were further examined using extended X-ray absorption fine structure (EXAFS). As shown in Fig. 3f, the main peaks of the Pt L_3-edge are located at 1.98 Å and 2.7 Å, corresponding to Pt-O and Pt-Pt/Pt-Ru coordination, respectively. The Pt-Pt/Ru coordination shell is slightly shorter than the Pt-Pt bond in Pt foil (2.8 Å). Similarly, the EXAFS of the Ru K-edge in PO-$Pt_{70}Ru_{30}$ shows a prominent peak at 2.7 Å, which is longer than the 2.4 Å Ru-Ru bond in Ru foil, and can be attributed to Ru-Pt/Ru-Ru coordination (Fig. 3h) [57,59,60] Moreover, the dominant peak between 1 and 2 Å in partially oxidized $Pt_{70}Ru_{30}$ is attributed to the coordination between Ru species and oxygen atoms.As shown in Fig. 3i, the Pt-Pt bond in Pt foil exhibits a principal intensity of around 10.8 $Å^{-1}$, which is higher than the principal intensity observed in PO-$Pt_{70}Ru_{30}$ (ranging from 6.1 to 9.2 $Å^{-1}$) [61,62]. Similarly, the principal intensity of Ru in PO-$Pt_{70}Ru_{30}$ is reduced to 8.2 $Å^{-1}$ compared to Ru foil (9.1 $Å^{-1}$), further confirming the strong interaction between Pt and Ru atoms in the alloy (Fig. 3j) [63]. In addition, WT analysis further proved the presence of Pt-O and Ru-O bonds in PO-$Pt_{70}Ru_{30}$.

3.3. Electrochemical performance

The electrocatalytic HER performance of all partially oxidized PtRu materials was evaluated using LSV scans at 5 mV s^{-1} in 1 M KOH, with commercial Pt/C as a reference (Fig. 4a). Notably, all partially oxidized PtRu materials show a more rapid increase in activity as the overpotential rises compared to commercial Pt/C, due to their enhanced HER kinetics. Among them, PO-$Pt_{70}Ru_{30}$ showed the highest activity, achieving a low overpotential of just 11 mV to deliver a current density of 10 mA cm^{-2} (Fig. 4b). This performance significantly surpasses that of PO-$Pt_{90}Ru_{10}$ (21 mV), PO-$Pt_{80}Ru_{20}$ (16 mV), and PO-$Pt_{60}Ru_{40}$ (28 mV), positioning it among the leading catalysts reported to date. Additionally, PO-$Pt_{70}Ru_{30}$ required only 123 mV and 196 mV to reach high current densities of 500 mA cm^{-2} and 1 A cm^{-2}, respectively (Fig. S24). The enhanced performance of PO-$Pt_{70}Ru_{30}$ can be attributed to its interconnected nanoparticles and optimized oxidation state, which facilitate efficient mass transfer and improve reaction kinetics during

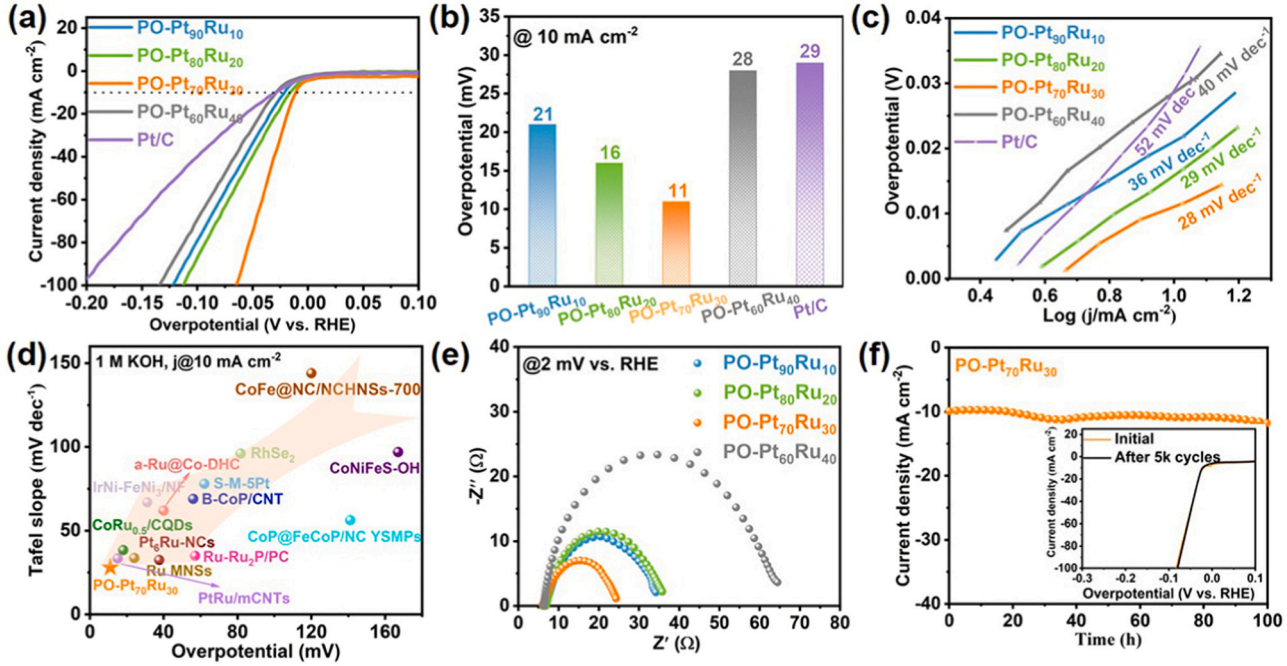

Fig. 4. Electrocatalytic behaviors of catalysts for HER. (a) HER polarization curve of partially oxidized PtRu materials, (b) overpotentials at current densities of 10 mA cm^{-2}, (c) Tafel slop, (d) comparison of overpotentials at 10 mA cm^{-2} in 1 M KOH with other reported alkaline HER electrocatalysts. (e) Nyquist plot of partially oxidized PtRu catalysts in 1 M KOH. (f) Chronoamperometry test of PO-$Pt_{70}Ru_{30}$ for alkaline HER (the inset shows the LSV curves before and after 5000 CV tests).

the HER process. The Tafel plots in Fig. 4c further reveal that PO-$Pt_{70}Ru_{30}$ has an impressively low Tafel slope of 26 mV dec^{-1}, significantly better than that of commercial Pt/C (52 mV dec^{-1}), as well as PO-$Pt_{90}Ru_{10}$ (34 mV dec^{-1}), PO-$Pt_{80}Ru_{20}$ (38 mV dec^{-1}), and PO-$Pt_{60}Ru_{40}$ (44 mV dec^{-1}), indicating its rapid HER kinetics. In fact, compared with previously reported Pt-based alkaline HER electrocatalysts, the low overpotential at 10 mA cm^{-2} and Tafel slope of PO-$Pt_{70}Ru_{30}$ exhibit competitive HER activity (Fig. 4d and Table S1) [64]. This enhanced reaction rate is further supported by EIS measurements, which reveal that PO-$Pt_{70}Ru_{30}$ has the lowest charge transfer resistance among the samples (Fig. 4e). The ECSA was estimated from the integrated charge of the hydrogen desorption region in the CV curve. As shown in Fig. S25, the ECSA values for PO-$Pt_{90}Ru_{10}$, PO-$Pt_{80}Ru_{20}$, PO-$Pt_{70}Ru_{30}$, and PO-$Pt_{60}Ru_{40}$ were 58.2 m^2 g^{-1}, 58.8 m^2 g^{-1}, 61.3 m^2 g^{-1}, and 67.1 m^2 g^{-1}, respectively, which correlate with the morphological changes shown in Fig. 3c-f. Notably, although PO-$Pt_{60}Ru_{40}$ had the largest ECSA, it exhibited lower HER catalytic activity compared to PO-$Pt_{70}Ru_{30}$, suggesting that a larger ECSA is not the sole factor determining alkaline HER performance. The superior HER activity of PO-$Pt_{70}Ru_{30}$ is further demonstrated by its mass activity, which is 2.16, 2.45, and 2.67 times greater than that of PO-$Pt_{90}Ru_{10}$, PO-$Pt_{80}Ru_{20}$, and PO-$Pt_{60}Ru_{40}$, respectively, at 50 mV vs. RHE (normalized to the metal Pt mass; Fig. S26a). It is worth mentioning that the mass activity of PO-$Pt_{70}Ru_{30}$ at 50 and 100 mV overpotentials is 4.2 and 3.8 times that of commercial Pt/C (Fig. S26b). To further understand the intrinsic capability of the as-prepared catalysts, the turnover frequency (TOF) is calculated. The results in Fig. S27 show PO-$Pt_{70}Ru_{30}$ exhibits the highest TOF value in the entire potential range. Specifically, PO-$Pt_{70}Ru_{30}$ exhibits the TOF of 1.12 s^{-1} at an overpotential of 100 mV, which is much higher than those of PO-$Pt_{90}Ru_{10}$ (0.04 s^{-1}), PO-$Pt_{80}Ru_{20}$ (0.28 s^{-1}) and PO-$Pt_{60}Ru_{40}$ (0.03 s^{-1}), demonstrating the superior intrinsic catalytic activity of PO-$Pt_{70}Ru_{30}$ for alkaline HER. To evaluate the durability of PO-$Pt_{70}Ru_{30}$ for HER, a chronopotentiometric test was conducted at a static overpotential in 1 M KOH. In the long-term stability test of 100 h, the current density of PO-$Pt_{70}Ru_{30}$ showed no obvious decreasing trend (Fig. 4f). Moreover, the LSV plots before and after 5000 CV cycles, shown in the inset of Fig. 4f, further confirm the stable properties of PO-$Pt_{70}Ru_{30}$. The catalytic stability of PO-$Pt_{70}Ru_{30}$ was also assessed at a higher current density of 400 mA cm^{-2}, where 91 % of the initial potential was retained over 20 h (Fig. S29a). After stability testing, characterizations, including high-resolution TEM images, EDX elemental mapping, XRD, Raman spectroscopy, and XPS have been conducted, which showed that the morphology, crystal structure, and surface electronic structure of partially oxidized $Pt_{70}Ru_{30}$ were well preserved (Fig. S30 and 31). Only 0.0032 μg mL^{-1} Ru dissolution was detected in the electrolyte, indicating that PO-$Pt_{70}Ru_{30}$ has excellent structural stability for alkaline HER. The excellent stability may be related to the anisotropic two-dimensional sheet structure of PO-$Pt_{70}Ru_{30}$, which largely delays the electrochemical dissolution and ripening process of Pt and Ru and improves the stability of alkaline HER. These results further confirm its exceptional catalytic activity and stability under alkaline HER conditions, attributed to the unique structure, which not only offers a larger exposed surface area and more active sites but also enhances the diffusion and transport of reactants, intermediates, and products. Additionally, the presence of partially oxidized Pt and Ru species serves as active sites for both water adsorption and H* reactions, significantly accelerating the alkaline HER process.

3.4. Kinetics and reaction mechanism for alkaline HER

The superior alkaline HER activity of PO-$Pt_{70}Ru_{30}$ compared to other PtRu alloy ratios suggests that its morphology, composition, and oxidation states play a critical role, with the partially oxidized Pt and Ru species likely serving as active sites for water dissociation and hydrogen adsorption. To further investigate the impact of surface oxidation states on alkaline HER activity, we modified the surface oxidation of PO-$Pt_{70}Ru_{30}$ through different annealing conditions. Specifically, we obtained reduced and further oxidized PO-$Pt_{70}Ru_{30}$ samples (referred to as $Pt_{70}Ru_{30}$-reduced and $Pt_{70}Ru_{30}$-oxidized) by heat-treating them in H_2/Ar and air for 2 h, respectively. The XRD results in Fig. S32 show that $Pt_{70}Ru_{30}$-reduced retains similar dominant peaks to PO-$Pt_{70}Ru_{30}$, indicating the alloy properties were preserved after treatment. In contrast, the predominant peaks of $Pt_{70}Ru_{30}$-oxidized shifted from alloy peaks to metal oxide peaks. Additionally, high-resolution Pt 4 f and Ru 3p spectra in Fig. S33a and 33b reveal that only metallic species are present in $Pt_{70}Ru_{30}$-reduced, suggesting that both Pt and Ru were fully reduced to their metallic states. Conversely, only oxidized Pt and Ru species were observed in $Pt_{70}Ru_{30}$-oxidized. The electrochemical performance (Fig. S34) shows that the alkaline HER activity decreased from 11 mV for PO-$Pt_{70}Ru_{30}$ to 47 mV and 104 mV for $Pt_{70}Ru_{30}$-reduced and $Pt_{70}Ru_{30}$-oxidized, respectively. These results indicate that the partially oxidized Pt and Ru species are crucial for achieving high alkaline HER activity.

We further conducted *in-situ* ATR-SEIRAS and Raman spectroscopy to investigate how the partially oxidized Pt and Ru species enhance alkaline HER activity. Since proton supply from water dissociation is essential for alkaline HER, the water adsorption and dissociation capabilities are critical for efficient electrocatalysis. The *in-situ* ATR-SEIRAS results for PO-$Pt_{70}Ru_{30}$, shown in Fig. 5a, reveal peaks near 3400 cm^{-1} corresponding to the O-H stretching vibration mode ($\nu_{O\text{-}H}$) of H_2O, while the peak around 1640 cm^{-1} corresponds to the H-O-H bending vibration mode ($\delta_{H\text{-}O\text{-}H}$) [65,66]. As the potential decreased from 0 to −0.35 V, the intensities of the $\nu_{O\text{-}H}$ and $\delta_{H\text{-}O\text{-}H}$ vibration peaks gradually increased, indicating enhanced water adsorption and dissociation on the surface of PO-$Pt_{70}Ru_{30}$ as the potential changed. In contrast, while an increasing trend was observed for the $\nu_{O\text{-}H}$ vibration peak on $Pt_{70}Ru_{30}$-oxidized, there was almost no change in the $\delta_{H\text{-}O\text{-}H}$ vibration peak (Fig. 5c), suggesting that the HER activity on $Pt_{70}Ru_{30}$-oxidized is limited by slow water dissociation kinetics. Additionally, the $\nu_{O\text{-}H}$ and $\delta_{H\text{-}O\text{-}H}$ vibration peaks for $Pt_{70}Ru_{30}$-reduced remained relatively weak across all potential ranges, indicating a lower capability for water adsorption and dissociation (Fig. 5b).

In-situ Raman spectroscopy was performed to investigate changes in interfacial water during the alkaline HER process [67]. The Raman spectra of PO-$Pt_{70}Ru_{30}$, $Pt_{70}Ru_{30}$-reduced, and $Pt_{70}Ru_{30}$-oxidized, shown in Fig. 5d-f, display a broad peak in the range of 3000–3700 cm^{-1}, corresponding to the OH stretching mode ($\nu_{O\text{–}H}$) of interfacial water [68,69]. Furthermore, the Raman peak can be decomposed into three O-H stretching modes of interfacial water using Gaussian fitting. The peaks at ~3225 cm^{-1} and ~3450 cm^{-1} correspond to four hydrogen-bonded water (V1) and two hydrogen-bonded water (V2), respectively, both representing active water molecules that are conducive to the HER process. The higher wavenumber peak at ~3615 cm^{-1} is associated with K^+-hydrated water and is attributed to the dangling O-H bonds of inactive water molecules at the interface (V3) [70,71]. As the potential decreases from 0 to -0.50 V, the V3 peak intensity of PO-$Pt_{70}Ru_{30}$ gradually diminishes, indicating effective water dissociation on its surface (Fig. 5g). In contrast, the V3 peak intensity of $Pt_{70}Ru_{30}$-reduced increases, suggesting that more inactive water molecules accumulate on the $Pt_{70}Ru_{30}$-reduced surface (Fig. 5h). The V3 peak intensity of $Pt_{70}Ru_{30}$-oxidized shows no significant change (Fig. 5i). These *in-situ* Raman results indicate that PO-$Pt_{70}Ru_{30}$ facilitates the breaking of H-O-H bonds, providing sufficient H* for the subsequent Volmer step in the HER process. The *in-situ* ATR-SEIRAS and Raman spectroscopy results of partially oxidized Pt and Ru showed gradually enhanced $\nu_{O\text{-}H}$ and $\delta_{H\text{-}O\text{-}H}$ vibration peaks and gradually weakened inactive water molecules hanging O-H bonds, which indicated that partially oxidized Pt and Ru promoted the adsorption of active H_2O molecules and accelerated the dissociation of H-OH bonds. This is highly consistent with the DFT results, which indicate that both partially oxidized Pt and Ru species act as active sites for H_2O adsorption and H* generation, thereby synergistically enhancing the alkaline HER

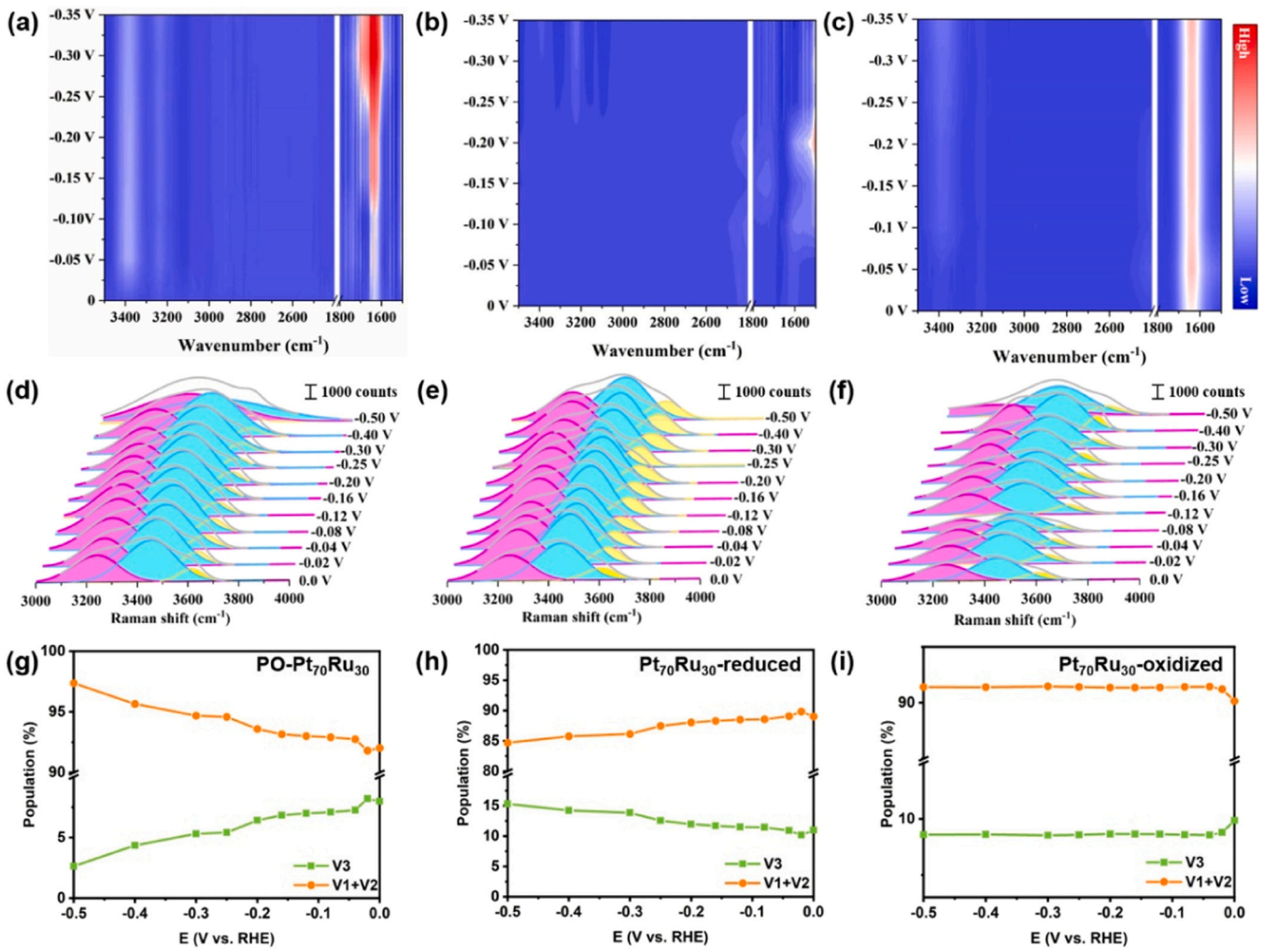

Fig. 5. *In-situ* ATR-SEIRAS contour plots of (a-c) the PO-$Pt_{70}Ru_{30}$, $Pt_{70}Ru_{30}$-reduced and $Pt_{70}Ru_{30}$-oxidized at different applied potentials from 0 to -0.35 V. *In-situ* Raman spectra of interfacial water at (d-f) PO-$Pt_{70}Ru_{30}$, $Pt_{70}Ru_{30}$-reduced and $Pt_{70}Ru_{30}$-oxidized surfaces, Gaussian fits of three peaks of V1, V2, and V3 are shown in red, blue, and green, respectively. (g-i) The ratio of activated water molecules/inactivated water molecules [(V1 + V2)/V3] on PO-$Pt_{70}Ru_{30}$, $Pt_{70}Ru_{30}$-reduced and $Pt_{70}Ru_{30}$-oxidized over HER potentials.

kinetics.

4. Conclusions

In summary, we have demonstrated that the PtRu alloys with optimized Pt/Ru ratio and oxidation state play a significant role in boosting the alkaline HER performance. The achieved $Pt_{70}Ru_{30}$ with 3 O surface coverage can not only significantly lowered the energy barrier of the rate-determining step (RDS) for alkaline HER, but also enable both partially oxidized Pt and Ru species to serve as active sites for water adsorption and H* reactions, which highly facilitate the alkaline HER process. Moreover, the introduction of Ru atoms and the partially oxidized properties improved the d-band center of Pt, which optimizes $\triangle G_{H^*}$ and results in rapid conversion of H* adsorbed on the Pt surface. Direct experimental evidence shows that PO-$Pt_{70}Ru_{30}$ synthesized by urea decomposition-assisted hydrothermal method and rapid thermal treatment method has exhibited the best HER activity, with an ultra-low overpotential of 11 mV to achieve a current density of 10 mA cm^{-2} and a low Tafel slope of 28 mV dec^{-1}, which is superior to those of commercial Pt/C and most alkaline HER electrocatalysts reported in recent years. It maintains stability in tests for up to 100 h, highlighting the robust stability and great potential for water electrolysis applications. Furthermore, in situ characterizations determined that PO-$Pt_{70}Ru_{30}$ possesses a fast water dissociation process, thereby reducing the rate-determining step and achieving rapid H_2 generation. This work not only demonstrates that even slight changes in the metal ratio and oxidation state can significantly impact catalytic performance but also maximizes the roles of Ru and Pt as active sites for alkaline HER, offering new insights into the design of efficient alloy electrocatalysts for energy conversion reactions.

Authors' contributions

The manuscript was written through contributions of all authors. All authors have given approval to the final version of the manuscript. Xianjun Cao and Limeng Sun have contributed equally to this work.

Declaration of Competing Interest

The authors declare the following financial interests/personal relationships which may be considered as potential competing interests: Hao Liu reports financial support was provided by Australian Research Council. If there are other authors, they declare that they have no known competing financial interests or personal relationships that could have appeared to influence the work reported in this paper.

Acknowledgements

This work was supported by the National Natural Science Foundation of China (22209103), the Australian Research Council (DE240100868), CSIRO "International Hydrogen Research Collaboration Program-RESEARCH FELLOWSHIPS", UTS Collaboration Scheme and the Post-doctoral Fellowship Program of CPSF (GZC20240974). Authors thanks for the support from "Joint International Laboratory on Environmental and Energy Frontier Materials" and the "Innovation Research Team of High-Level Local Universities in Shanghai". Part of this work was carried out at the X-ray absorption spectroscopy (XAS) beamline (beamtime: M22038) at the Australian Synchrotron. The authors especially acknowledge the operational support of Dr. Bernt Johannessen from ANSTO for collecting and processing XAS data.

Appendix A. Supporting information

Supplementary data associated with this article can be found in the online version at doi:10.1016/j.apcatb.2025.125415.

Data availability

No data was used for the research described in the article.

References

[1] A. Olabi, A.A. Abdelghafar, A. Baroutaji, E.T. Sayed, A.H. Alami, H. Rezk, M. A. Abdelkareem, Large-vscale hydrogen production and storage technologies: current status and future directions, Int. J. Hydrog. Energy 46 (2021) 23498–23528, https://doi.org/10.1016/j.ijhydene.2020.10.110.

[2] J. Huo, Z. Shen, X. Cao, L. Li, Y. Zhao, H. Liu, G. Wang, Macro/micro-environment regulating carbon-supported single-atom catalysts for hydrogen/oxygen conversion reactions, Small 18 (2022) 2202394, https://doi.org/10.1002/smll.202202394.

[3] J.N. Tiwari, S. Sultan, C.W. Myung, T. Yoon, N. Li, M. Ha, A.M. Harzandi, H. J. Park, D.Y. Kim, S.S. Chandrasekaran, W.G. Lee, V. Vij, H. Kang, T.J. Shin, H. S. Shin, G. Lee, Z. Lee, K.S. Kim, Multicomponent electrocatalyst with ultralow Pt loading and high hydrogen evolution activity, Nat. Energy 3 (2018) 773–782, https://doi.org/10.1038/s41560-018-0209-x.

[4] L. Ring, B.G. Pollet, M. Chatenet, S. Abbou, K. Küpper, M. Schmidt, M. Huck, A. Gries, M. Steinhart, H. Schäfer, From bad electrochemical practices to an environmental and waste reducing approach for the generation of active hydrogen evolving electrodes, Angew. Chem. Int. Ed. 58 (2019) 17383–17392, https://doi.org/10.1002/anie.201908649.

[5] J. Guo, J. Huo, Y. Liu, W. Wu, Y. Wang, M. Wu, H. Liu, G. Wang, Nitrogen-doped porous carbon supported nonprecious metal single-atom electrocatalysts: from synthesis to application, Small Methods 3 (2019) 1900159, https://doi.org/10.1002/smtd.201900159.

[6] F. Wu, F. Tian, M. Li, S. Geng, L. Qiu, L. He, L. Li, Z. Chen, Y. Yu, W. Yang, Y. Hou, Engineering lattice oxygen regeneration of NiFe layered double hydroxide enhances oxygen evolution catalysis durability, Angew. Chem. Int. Ed. 64 (2025) e202413250, https://doi.org/10.1002/anie.202413250.

[7] J. Gao, H. Tao, B. Liu, Progress of nonprecious-metal-based electrocatalysts for oxygen evolution in acidic media, Adv. Mater. 33 (2021) 2003786, https://doi.org/10.1002/adma.202003786.

[8] W. Yu, Z. Chen, Y. Fu, W. Xiao, B. Dong, Y. Chai, Z. Wu, L. Wang, Superb all-pH hydrogen evolution performances powered by ultralow Pt-decorated hierarchical Ni-Mo porous microcolumns, Adv. Funct. Mater. 33 (2023) 2210855, https://doi.org/10.1002/adfm.202210855.

[9] S.S. Kumar, V. Himabindu, Hydrogen production by pem water electrolysis-a review, Mater. Sci. Energy Technol. 2 (2019) 442–454, https://doi.org/10.1016/j.mset.2019.03.002.

[10] J. Islam, S.-K. Kim, P.T. Thien, M.-J. Kim, H.-S. Cho, W.-C. Cho, C.-H. Kim, C. Lee, J.H. Lee, Enhancing the activity and durability of iridium electrocatalyst supported on boron carbide by tuning the chemical state of iridium for oxygen evolution reaction, J. Power Sources 512 (2021) 230506, https://doi.org/10.1016/j.jpowsour.2021.230506.

[11] F. Jiang, Y. Li, Y. Pan, Design principles of single-atom catalysts for oxygen evolution reaction: from targeted structures to active sites, Adv. Mater. 36 (2024) 2306309, https://doi.org/10.1002/adma.202306309.

[12] D. Gao, S. Ji, V. Linkov, R. Wang, High current water electrolysis catalyst based on Fe/Ni (Ni/Fe) hierarchically structured electrode, Int. J. Hydrog. Energy 47 (2022) 37831–37839, https://doi.org/10.1016/j.ijhydene.2022.08.273.

[13] R.R. Raja Sulaiman, W.Y. Wong, K.S. Loh, Recent developments on transition metal-based electrocatalysts for application in anion exchange membrane water electrolysis, Int. J. Energy Res. 46 (2022) 2241–2276, https://doi.org/10.1002/er.7380.

[14] J. Chen, M. Aliasgar, F.B. Zamudio, T. Zhang, Y. Zhao, X. Lian, L. Wen, H. Yang, W. Sun, S.M. Kozlov, W. Chen, L. Wang, Diversity of platinum-sites at platinum/fullerene interface accelerates alkaline hydrogen evolution, Nat. Commun. 14 (2023) 1711, https://doi.org/10.1038/s41467-023-37404-0.

[15] X. Cao, J. Huo, L. Li, J. Qu, Y. Zhao, W. Chen, C. Liu, H. Liu, G. Wang, Recent advances in engineered Ru-based electrocatalysts for the hydrogen/oxygen conversion reactions, Adv. Energy Mater. 12 (2022) 2202119, https://doi.org/10.1002/aenm.202202119.

[16] J. Liu, X. Sun, Y. Du, Y. Liu, W. Wang, D. Chen, R. Zhang, L. Wang, Ru-triggered domino effect constructs a local acid-like environment to achieve the ampere-level current density of a/c-Ru-FeP/IF electrode for alkaline HER, Appl. Catal. B Environ. Energy 366 (2025) 125030, https://doi.org/10.1016/j.apcatb.2025.125030.

[17] P.-J. Deng, Y. Wang, Y. Liu, J. Lu, H.-P. Liang, Heat-induced aliquation and phosphating of nickel as efficient catalysts for hydrogen evolution in alkaline seawater, Mater. Today Energy 44 (2024) 101635, https://doi.org/10.1016/j.mtener.2024.101635.

[18] J. Wu, Z. Zhai, S. Yin, S. Wang, General formation of interfacial assembled hierarchical micro-nano arrays for biomass upgrading-coupled hydrogen production, Adv. Funct. Mater. 34 (2024) 2308198, https://doi.org/10.1002/adfm.202308198.

[19] H. Xu, X. Chen, Z. Wei, G. Qian, P. Tsiakaras, Novel V-doped $CuCoN_{0.6}/Ni_4N$ heterojunction for boosting water electrolysis by facilitating water dissociation and H* adsorption-desorption kinetics, Int. J. Hydrog. Energy 80 (2024) 1432–1440, https://doi.org/10.1016/j.ijhydene.2024.07.186.

[20] G. Qian, Y. Wang, L. Li, M. Lu, C. Chen, D. Min, Z. Wei, P. Tsiakaras, Strategies for tuning tensile strain and localized electrons in a Mo-doped NiCoCu alloy for enhancing ampere-level current density HER performance, Adv. Funct. Mater. 34 (2024) 2404055, https://doi.org/10.1002/adfm.202404055.

[21] J. Chen, T. Yu, Z. Zhai, G. Qian, S. Yin, Coupling interface engineering with electronic interaction toward high-efficiency H_2 evolution in pH-universal electrolytes, J. Energy Chem. 80 (2023) 535–541, https://doi.org/10.1016/j.jechem.2023.01.060.

[22] Z. Wu, Q. Li, G. Xu, W. Jin, W. Xiao, Z. Li, T. Ma, S. Feng, L. Wang, Microwave phosphine-plasma-assisted ultrafast synthesis of halogen-doped Ru/RuP_2 with surface intermediate adsorption modulation for efficient alkaline hydrogen evolution reaction, Adv. Mater. 36 (2024) 2311018, https://doi.org/10.1002/adma.202311018.

[23] L. Liu, Y. Wang, Y. Zhao, Y. Wang, Z. Zhang, T. Wu, W. Qin, S. Liu, B. Jia, H. Wu, D. Zhang, X. Qu, M. Chhowalla, M. Qin, Ultrahigh Pt-mass-activity hydrogen evolution catalyst electrodeposited from bulk Pt, Adv. Funct. Mater. 32 (2022) 2112207, https://doi.org/10.1002/adfm.202112207.

[24] Y. Yan, J. Lin, T. Xu, B. Liu, K. Huang, L. Qiao, S. Liu, J. Cao, S.C. Jun, Y. Yamauchi, J. Qi, Atomic-level platinum filling into Ni-vacancies of dual-deficient nio for boosting electrocatalytic hydrogen evolution, Adv. Energy Mater. 12 (2022) 2200434, https://doi.org/10.1002/aenm.202200434.

[25] Y. Zhao, P.V. Kumar, X. Tan, X. Lu, X. Zhu, J. Jiang, J. Pan, S. Xi, H.Y. Yang, Z. Ma, T. Wan, D. Chu, W. Jiang, S.C. Smith, R. Amal, Z. Han, X. Lu, Modulating Pt-O-Pt atomic clusters with isolated cobalt atoms for enhanced hydrogen evolution catalysis, Nat. Commun. 13 (2022) 2430, https://doi.org/10.1038/s41467-022-30155-4.

[26] G. Gao, Z. Sun, X. Chen, G. Zhu, B. Sun, Y. Yamauchi, S. Liu, Recent advances in Ru/Ir-based electrocatalysts for acidic oxygen evolution reaction, Appl. Catal. B Environ. Energy 343 (2024) 123584, https://doi.org/10.1016/j.apcatb.2023.123584.

[27] Y. Wang, W. Wu, R. Chen, C. Lin, S. Mu, N. Cheng, Reduced water dissociation barrier on constructing $Pt\text{-}Co/CoO_x$ interface for alkaline hydrogen evolution, Nano Res. 15 (2022) 4958–4964, https://doi.org/10.1007/s12274-022-4128-6.

[28] B. Ruqia, S.-I. Choi, Pt and $Pt\text{-}Ni(OH)_2$ electrodes for the hydrogen evolution reaction in alkaline electrolytes and their nanoscaled electrocatalysts, ChemSusChem 11 (2018) 2643–2653, https://doi.org/10.1002/cssc.201800781.

[29] J. Zhang, X. Zhang, C. Shi, G. Xia, H. Li, P. Wang, L. Di, Plasma synthesis of defect-rich flexible carbon cloth decorated with PtRu alloyed nanoclusters for highly efficient pH-universal electrocatalytic hydrogen evolution, Nanoscale 14 (2022) 15942–15949, https://doi.org/10.1039/D2NR04369F.

[30] I.T. McCrum, M.T.M. Koper, The role of adsorbed hydroxide in hydrogen evolution reaction kinetics on modified platinum, Nat. Energy 5 (2020) 891–899, https://doi.org/10.1038/s41560-020-00710-8.

[31] R. Jiang, Y. Da, G. Chen, Z. Tian, Y. Xiao, Y. Cao, H. Wu, J. Zhang, X. Han, Y. Deng, W. Hu, Synergy of torsion strained and ligand effect for relay acceleration of industrial high-pH hydrogen evolution, Adv. Funct. Mater. 33 (2023) 2305893, https://doi.org/10.1002/adfm.202305893.

[32] S. Shen, Z. Hu, H. Zhang, K. Song, Z. Wang, Z. Lin, Q. Zhang, L. Gu, W. Zhong, Highly active Si sites enabled by negative valent Ru for electrocatalytic hydrogen evolution in LaRuSi, Angew. Chem. Int. Ed. Engl. 61 (2022) e202206460, https://doi.org/10.1002/anie.202206460.

[33] H. Sun, X. Xu, H. Kim, Z. Shao, W. Jung, Advanced electrocatalysts with unusual active sites for electrochemical water splitting, InfoMat 6 (2024) e12494, https://doi.org/10.1002/inf2.12494.

[34] H. Tan, B. Tang, Y. Lu, Q. Ji, L. Lv, H. Duan, N. Li, Y. Wang, S. Feng, Z. Li, C. Wang, F. Hu, Z. Sun, W. Yan, Engineering a local acid-like environment in alkaline medium for efficient hydrogen evolution reaction, Nat. Commun. 13 (2022) 2024, https://doi.org/10.1038/s41467-022-29710-w.

[35] Y. Dang, T. Wu, H. Tan, J. Wang, C. Cui, P. Kerns, W. Zhao, L. Posada, L. Wen, S. L. Suib, Partially reduced Ru/RuO_2 composites as efficient and pH-universal

electrocatalysts for hydrogen evolution, Energ. Environ. Sci. 14 (2021) 5433–5443, https://doi.org/10.1039/D1EE02380B.
[36] D. Cao, H. Xu, H. Li, C. Feng, J. Zeng, D. Cheng, Volcano-type relationship between oxidation states and catalytic activity of single-atom catalysts towards hydrogen evolution, Nat. Commun. 13 (2022) 5843, https://doi.org/10.1038/s41467-022-33589-y.
[37] B. Pang, X. Liu, T. Liu, T. Chen, X. Shen, W. Zhang, S. Wang, T. Liu, D. Liu, T. Ding, Laser-assisted high-performance PtRu alloy for pH-universal hydrogen evolution, Energ. Environ. Sci. 15 (2022) 102, https://doi.org/10.1039/D1EE02518J.
[38] S. Zhu, X. Qin, F. Xiao, S. Yang, Y. Xu, Z. Tan, J. Li, J. Yan, Q. Chen, M. Chen, M. Shao, The role of ruthenium in improving the kinetics of hydrogen oxidation and evolution reactions of platinum, Nat. Catal. 4 (2021) 711–718, https://doi.org/10.1038/s41929-021-00663-5.
[39] X. Cao, L. Gao, J. Qu, L. Li, Y. Xie, Y. Zhao, G. Wang, H. Liu, Modulating electronic structure of PtCo-Pt_{rich} nanowires with Ru atoms for boosted hydrogen evolution catalysis, Small, n/a 2302639, https://doi.org/10.1002/smll.202302639.
[40] J. Hao, Z. Zhuang, K. Cao, G. Gao, C. Wang, F. Lai, S. Lu, P. Ma, W. Dong, T. Liu, M. Du, H. Zhu, Unraveling the electronegativity-dominated intermediate adsorption on high-entropy alloy electrocatalysts, Nat. Commun. 13 (2022) 2662, https://doi.org/10.1038/s41467-022-30379-4.
[41] H. Chen, M. Yang, J. Liu, G. Lu, X. Feng, Insight into the effects of electronegativity on the H_2 atalytic activation for CO_2 hydrogenation: four transition metal cases from a DFT study, Catal. Sci. Technol. 10 (2020) 5641–5647, https://doi.org/10.1039/D0CY01009J.
[42] D. Kobayashi, H. Kobayashi, D. Wu, S. Okazoe, K. Kusada, T. Yamamoto, T. Toriyama, S. Matsumura, S. Kawaguchi, Y. Kubota, S.M. Aspera, H. Nakanishi, S. Arai, H. Kitagawa, Significant enhancement of hydrogen evolution reaction activity by negatively charged Pt through light doping of W, J. Am. Chem. Soc. 142 (2020) 17250–17254, https://doi.org/10.1021/jacs.0c07143.
[43] S. Zhang, L. Yin, S. Wang, J.-C. Liu, Y. Zhang, Y. Wen, Q. Zhang, Y. Du, Ternary rare earth alloy $Pt_{3-x}Ir_xSc$ nanoparticles modulate negatively charged Pt via charge transfer to facilitate pH-universal hydrogen evolution, ACS Nano 17 (2023) 23103–23114, https://doi.org/10.1021/acsnano.3c08921.
[44] M. Maji, S. Dutta, R. Jena, A. Dey, T.K. Maji, S.K. Pati, S. Bhattacharyya, Hydrogen evolution in neutral media by differential intermediate binding at charge-modulated sites of a bimetallic alloy electrocatalyst, Angew. Chem. Int. Ed. 63 (2024) e202403697, https://doi.org/10.1002/anie.202403697.
[45] G. Qian, Y. Wang, L. Li, M. Lu, C. Chen, D. Min, Z. Wei, P. Tsiakaras, Strategies for tuning tensile strain and localized electrons in a Mo-doped NiCoCu alloy for enhancing ampere-level current density her performance, Adv. Funct. Mater. (2024) 2404055, https://doi.org/10.1002/adfm.202404055.
[46] J. Kostera, J. McGarry, A.A. Pacheco, Enzymatic interconversion of ammonia and nitrite: the right tool for the job, Biochemistry 49 (2010) 8546–8553, https://doi.org/10.1021/bi1006783.
[47] L. Li, Y. He, Z. Zhang, Y. Liu, Nitrogen isotope fractionations among gaseous and aqueous NH_4^+, NH_3, N_2, and metal-ammine complexes: Theoretical calculations and applications, Geochim. Cosmochim. Acta 295 (2021) 80–97, https://doi.org/10.1016/j.gca.2020.12.010.
[48] Q. Yang, L. Shi, B. Yu, J. Xu, C. Wei, Y. Wang, H. Chen, Facile synthesis of ultrathin Pt-Pd nanosheets for enhanced formic acid oxidation and oxygen reduction reaction, J. Mater. Chem. A 7 (2019) 18846–18851, https://doi.org/10.1039/C9TA03945G.
[49] Q. Mao, X. Mu, K. Deng, H. Yu, Z. Wang, Y. Xu, X. Li, L. Wang, H. Wang, Multisite synergism-induced electron regulation of high-entropy alloy metallene for boosting alkaline hydrogen evolution reaction, Adv. Funct. Mater. 33 (2023) 2304963, https://doi.org/10.1002/adfm.202304963.
[50] T. Onodera, S. Suzuki, Y. Takamori, H. Daimon, Improved methanol oxidation activity and stability of well-mixed ptru catalysts synthesized by electroless plating method with addition of chelate ligands, Appl. Catal. A Gen. 379 (2010) 69–76, https://doi.org/10.1016/j.apcata.2010.03.003.
[51] C.M. Pelicano, M. Saruyama, R. Takahata, R. Sato, Y. Kitahama, H. Matsuzaki, T. Yamada, T. Hisatomi, K. Domen, T. Teranishi, Bimetallic synergy in ultrafine cocatalyst alloy nanoparticles for efficient photocatalytic water splitting, Adv. Funct. Mater. 32 (2022) 2202987, https://doi.org/10.1002/adfm.202202987.
[52] Y. Sang, R. Zhang, B. Xu, J. Yang, C. Zhao, H. Xu, Ultrafine and highly dispersed PtRu alloy on polyacrylic acid-grafted carbon nanotube@Tin oxide core/shell composites for direct methanol fuel cells, ACS Appl. Energy Mater. 5 (2022) 4179–4190, https://doi.org/10.1021/acsaem.1c03617.
[53] Z. Huang, S. Hu, M. Sun, Y. Xu, S. Liu, R. Ren, L. Zhuang, T.-S. Chan, Z. Hu, T. Ding, J. Zhou, L. Liu, M. Wang, Y.-C. Huang, N. Tian, L. Bu, B. Huang, X. Huang, Implanting oxophilic metal in PtRu nanowires for hydrogen oxidation catalysis, Nat. Commun. 15 (2024) 1097, https://doi.org/10.1038/s41467-024-45369-x.
[54] P. Kuang, Y. Wang, B. Zhu, F. Xia, C.-W. Tung, J. Wu, H.M. Chen, J. Yu, Pt single atoms supported on N-doped mesoporous hollow carbon spheres with enhanced electrocatalytic H_2-evolution activity, Adv. Mater. 33 (2021) 2008599, https://doi.org/10.1002/adma.202008599.
[55] G. Shu, Y. Lin, S. Wang, S. Zhang, L. Fan, C. Wang, C. Zhou, L. Song, L. Zheng, J. Zhang, K. Ma, H. Yue, Dynamic metal-support interaction-activated sub-nanometer Pt clusters on FeO_x supports for aqueous phase reforming and hydrogenolysis of glycerol, ACS Catal. 13 (2023) 8423–8436, https://doi.org/10.1021/acscatal.3c00415.
[56] Y. Chen, J. Li, N. Wang, Y. Zhou, J. Zheng, W. Chu, Plasma-assisted highly dispersed Pt single atoms on Ru nanoclusters electrocatalyst for pH-universal hydrogen evolution, Chem. Eng. J. 448 (2022) 137611, https://doi.org/10.1016/j.cej.2022.137611.
[57] Z. Niu, Z. Lu, Z. Qiao, S. Wang, X. Cao, X. Chen, J. Yun, L. Zheng, D. Cao, Robust Ru-VO2 bifunctional catalysts for all-pH overall water splitting, Adv. Mater. 36 (2024) 2310690, https://doi.org/10.1002/adma.202310690.
[58] K.L. Zhou, Z. Wang, C.B. Han, X. Ke, C. Wang, Y. Jin, Q. Zhang, J. Liu, H. Wang, H. Yan, Platinum single-atom catalyst coupled with transition metal/metal oxide heterostructure for accelerating alkaline hydrogen evolution reaction, Nat. Commun. 12 (2021) 3783, https://doi.org/10.1038/s41467-021-24079-8.
[59] L. Chen, X. Liang, D. Wang, Z. Yang, C. He, W. Zhao, J. Pei, Y. Xue, Platinum-ruthenium single atom alloy as a bifunctional electrocatalyst toward methanol and hydrogen oxidation reactions, ACS Appl. Mater. Interfaces 14 (2022) 27814–27822, https://doi.org/10.1021/acsami.2c02905.
[60] W. Zhao, C. Luo, Y. Lin, G.B. Wang, H.M. Chen, P. Kuang, J. Yu, Pt-Ru dimer electrocatalyst with electron redistribution for hydrogen evolution reaction, ACS Catal. 12 (2022) 5540, https://doi.org/10.1021/acscatal.2c00851.
[61] S. Tian, B. Wang, W. Gong, Z. He, Q. Xu, W. Chen, Q. Zhang, Y. Zhu, J. Yang, Q. Fu, C. Chen, Y. Bu, L. Gu, X. Sun, H. Zhao, D. Wang, Y. Li, Dual-atom Pt heterogeneous catalyst with excellent catalytic performances for the selective hydrogenation and epoxidation, Nat. Commun. 12 (2021) 3181, https://doi.org/10.1038/s41467-021-23517-x.
[62] N. Gong, H. He, H. Wan, H. Hou, Z. Zhou, Y. Yang, G. Qin, A. Yin, Y. Cai, X. Sun, Y. Li, Z. Cao, Insights into the electronic modulation of bimetallic Pt-Sn cluster for the selective hydrogenation of 1,3-butadiene, Catal. Sci. Technol. 13 (2023) 3313–3320, https://doi.org/10.1039/D3CY00016H.
[63] J. Li, C. Zhang, C. Zhang, H. Ma, Z. Guo, C. Zhong, M. Xu, X. Wang, Y. Wang, H. Ma, J. Qiu, Green electrosynthesis of 5,5′-azotetrazolate energetic materials plus energy-efficient hydrogen production using ruthenium single-atom catalysts, Adv. Mater. 34 (2022) 2203900, https://doi.org/10.1002/adma.202203900.
[64] C. Cai, K. Liu, Y. Zhu, P. Li, Q. Wang, B. Liu, S. Chen, H. Li, L. Zhu, H. Li, J. Fu, Y. Chen, E. Pensa, J. Hu, Y.R. Lu, T.S. Chan, E. Cortes, M. Liu, Optimizing hydrogen binding on Ru sites with RuCo alloy nanosheets for efficient alkaline hydrogen evolution, Angew. Chem. Int. Ed. 34 (2021) 202113664, https://doi.org/10.1002/anie.202113664.
[65] X. Yang, M. Xi, X. Guo, J. Shen, Z. Liu, H. Jiang, Y. Zhu, Ni-CeO_2 heterostructure promotes hydrogen evolution reaction via tuning of the O-H bond length of adsorbed water at the electrolyte/electrode interface, ChemSusChem 16 (2023) e202300348, https://doi.org/10.1002/cssc.202300348.
[66] K. Sun, X. Wu, Z. Zhuang, L. Liu, J. Fang, L. Zeng, J. Ma, S. Liu, J. Li, R. Dai, X. Tan, K. Yu, D. Liu, W.-C. Cheong, A. Huang, Y. Liu, Y. Pan, H. Xiao, C. Chen, Interfacial water engineering boosts neutral water reduction, Nat. Commun. 13 (2022) 6260, https://doi.org/10.1038/s41467-022-33984-5.
[67] Y.-L. Sun, X. Ji, X. Wang, Q.-F. He, J.-C. Dong, J.-B. Le, J.-F. Li, Visualization of electrooxidation on palladium single crystal surfaces via in situ Raman spectroscopy, Angew. Chem. Int. Ed. 63 (2024) e202408736, https://doi.org/10.1002/anie.202408736.
[68] Q. Dai, L. Wang, K. Wang, X. Sang, Z. Li, B. Yang, J. Chen, L. Lei, L. Dai, Y. Hou, Accelerated water dissociation kinetics by electron-enriched cobalt sites for efficient alkaline hydrogen evolution, Adv. Funct. Mater. 32 (2022) 2109556, https://doi.org/10.1002/adfm.202109556.
[69] X. Chen, X.-T. Wang, J.-B. Le, S.-M. Li, X. Wang, Y.-J. Zhang, P. Radjenovic, Y. Zhao, Y.-H. Wang, X.-M. Lin, J.-C. Dong, J.-F. Li, Revealing the role of interfacial water and key intermediates at ruthenium surfaces in the alkaline hydrogen evolution reaction, Nat. Commun. 14 (2023) 5289, https://doi.org/10.1038/s41467-023-41030-1.
[70] L. Wang, M. Ma, C. Zhang, H.-H. Chang, Y. Zhang, L. Li, H.-Y. Chen, S. Peng, Manipulating the microenvironment of single atoms by switching support crystallinity for industrial hydrogen evolution, Angew. Chem. Int. Ed. Engl. 136 (2024) e202317220, https://doi.org/10.1002/anie.202317220.
[71] J.-s Zhu, H. Yang, W. Zhang, Y. Mao, S.-s Lyu, J. Chen, An in situ raman study of intermediate adsorption engineering by high-index facet control during the hydrogen evolution reaction, Inorg. Chem. Front. 7 (2020) 1892–1899, https://doi.org/10.1039/D0QI00124D.